remote sensing

MDPI

Article

Evaluating Low-Cost GNSS Network Densification for Water-Vapor Tomography over an Urban Area: A Case Study over Lisbon

Rui Minez, João Catalão * and Pedro Mateus

Instituto Dom Luiz, Faculdade de Ciências, Universidade de Lisboa, Campo Grande, 1749-016 Lisbon, Portugal; fc55005@alunos.ciencias.ulisboa.pt (R.M.); pjmateus@ciencias.ulisboa.pt (P.M.)
* Correspondence: jcfernandes@ciencias.ulisboa.pt

Highlights

What are the main findings?

- Adding affordable receivers to a GNSS network enhances the reliability and measurement accuracy of water-vapor tomography, with the best overall results achieved through an optimal hybrid setup (permanent plus low-cost), especially for near-surface moisture and integrated water vapor.
- The geometry of the network strongly influences solution quality: higher station density improves detection of moisture variability associated with storms, whereas sparse or irregular configurations can cause inversion artifacts and vertical smoothing, reducing accuracy in the mid- and upper troposphere.

What are the implications of the main findings?

- Dense, cost-effective GNSS deployments can act as a practical tool for urban moisture monitoring and enhance the detection of low-level moisture buildup relevant to heavy rainfall and flash-flood nowcasting.
- The effective use of GNSS tomography in forecasting systems should focus on boundary-layer and column water vapor applications, while accounting for altitude-dependent uncertainty. Additionally, future advancements will rely on network densification and methodological improvements to better define upper-level humidity structures.

Abstract

This study evaluates GNSS water-vapor tomography across the Lisbon metropolitan area and explores how increasing network density with low-cost receivers improves three-dimensional humidity fields for meteorological applications. Three configurations were tested for December 2022, a month characterized by several rainfall events, including a severe urban-impacting one: (i) a hybrid setup combining permanent and low-cost stations (TOMO_PL), (ii) a dense network of only low-cost stations (TOMO_L), (iii) a sparse arrangement using only permanent stations (TOMO_P). Tomographic water vapor density fields were compared with independent references from the Weather Research and Forecasting (WRF) model, ERA 5 reanalysis, and radiosonde data. All products show the expected exponential decline in water vapor with increasing altitude. Tomography consistently underestimates moisture in the lowest 2.0 to 2.5 km and tends to overestimate it at higher levels, with a weaker correlation above mid-tropospheric heights. Vertical RMSE remains below 2 g m^{-3} for all solutions, but TOMO_P performs the worst due to weak and uneven spatial geometry. Time–height analysis reveals that densified setups

Check for updates

Academic Editor: Dongdong Wang

Received: 24 February 2026
Revised: 6 April 2026
Accepted: 13 April 2026
Published: 16 April 2026

Copyright: © 2026 by the authors. Licensee MDPI, Basel, Switzerland. This article is an open access article distributed under the terms and conditions of the Creative Commons Attribution (CC BY) license.

capture the changing moisture in the lower atmosphere, including increased near-surface humidity during December 11–13, when rainfall exceeded 120 mm in 24 h, although mid-level intrusions and dry layers observed by radiosondes are not captured. Mean PWV patterns show realistically low points over the Sintra mountain range and align best with TOMO_PL (spatial RMSE 0.6 g m^{-3}, bias 0.4 g m^{-3}, correlation 0.9), while TOMO_P creates artifacts that mimic mesoscale gradients. Categorized skill analysis shows the highest accuracy under high-moisture conditions and limited ability to detect dry conditions, with TOMO_PL showing the best overall performance against both ERA5 and WRF. Overall, low-cost densification significantly enhances boundary-layer humidity and PWV retrievals, supporting their use for urban heavy-rain monitoring and, with error-aware integration, for short-term forecasting.

Keywords: GNSS tomography; water vapor; low-cost GNSS stations

1. Introduction

The use of GNSS tomography has gained significant attention in recent years, as it provides a promising approach for monitoring water vapor with high spatial and temporal resolution, which is crucial for improving numerical weather prediction models, particularly for severe weather events such as storms with heavy rainfall [1,2].

The tropospheric delay affecting GNSS signals, mainly due to atmospheric water vapor, can be inverted to determine the integrated water vapor content along the signal's path. Therefore, measurements of signal delay serve as an indirect yet reliable way to estimate the water vapor along the propagation path. Based on this, a network of GNSS stations evenly distributed across the surface can serve as a tomographic system for the atmosphere, providing a 3D estimate of water vapor density. The concept was proposed and implemented by Flores et al. [3] using a network of GPS stations and further developed by [4]. However, the inversion of this tomographic system is ill-posed because it is underdetermined and sensitive to noise and modeling errors. This mainly results from the sparse and anisotropic geometry of GNSS ray paths, which limits the ability to resolve three-dimensional structures, especially horizontally. Additionally, discretizing the study volume into many voxels often leads to more unknowns than observations. These limitations, along with discretization effects and temporal variability, require regularization strategies and a priori constraints to produce stable, physically meaningful solutions [1].

To address the inherently ill-posed GNSS tomographic inversion, various stabilization strategies have been proposed in the literature. These approaches typically include regularization techniques [5] and the use of a priori information to constrain the solution space and reduce noise amplification caused by sparse, anisotropic ray coverage [4,6]. Time-recursive estimation methods, such as Kalman filtering, further improve solution stability by leveraging the temporal continuity of the atmosphere or ionosphere [7]. Additionally, optimized voxel parameterization and adaptive discretization schemes have been shown to improve the conditioning of the tomographic system by reducing the number of unknowns in poorly observed regions [8,9]. The integration of multi-GNSS constellations, supplementary data sources, and higher ground-based GNSS station density can significantly increase ray-path diversity and spatial coverage, thereby improving the observation geometry [10]. Recently, Miranda and Mateus [11] developed an algorithm that estimates the number of virtual GNSS signals from observed signals, ensuring that GNSS rays intersect all voxels. Overall, these strategies aim to achieve stable and physically meaningful tomographic reconstruc-

tion despite the fundamental limitations imposed by GNSS measurement geometry and data availability.

Among these strategies, station densification is especially crucial in urban environments where deploying dense GNSS networks can greatly improve the spatial resolution of tomographic reconstructions [12–14]. Urban areas offer favorable conditions for high receiver density, thereby increasing the number of available GNSS ray paths and improving sampling of the lower atmosphere [13]. Recent advancements in low-cost GNSS receiver technology have further increased the feasibility of such dense networks, making large-scale deployments more affordable [15]. Although low-cost receivers may produce higher noise measurements than geodetic-grade instruments, their wider spatial coverage and observational redundancy can partly offset these limitations when properly modeled [16]. Therefore, combining dense urban GNSS networks with low-cost receivers offers a promising approach to improve the conditioning of the tomographic system and enhance the robustness and resolution of GNSS tomographic solutions. An example of this approach is the GNSS network in Wroclaw, Poland, which successfully demonstrated the potential of such systems for high-resolution monitoring of atmospheric water vapor [17]. Similarly, dense GNSS networks with low-cost receivers have been studied in Switzerland for environmental monitoring, especially for estimating atmospheric water vapor and soil moisture [18]. Recently, the CentipedeRTK network, launched in 2019, aimed to provide free, real-time GNSS positioning with centimeter-level accuracy across mainland France. As of September 2024, the network included over 700 stations, mostly equipped with low-cost GNSS receivers and antennas, illustrating the scalability and practicality of dense, low-cost GNSS systems [19,20].

However, the impact of using different GNSS station types, including low-cost and geodetic-grade receivers, on the accuracy and reliability of tomographic results remains a key research question. Several studies have evaluated the reliability of low-cost dual-frequency GNSS receivers and antennas across various applications, using high-quality geodetic GNSS stations as a reference [21–25]. All conclude that low-cost equipment has a lower carrier-to-noise ratio (C/N_0) than geodetic instruments, but is suitable for applications such as monitoring, mapping, and positioning, even under demanding conditions [26]. Other studies investigate the capability of low-cost equipment to retrieve tropospheric delay [27–30]. While some doubts exist, all reach the same conclusion: low-cost receivers demonstrate high accuracy in atmospheric measurements.

This study aims to explore the potential of GNSS tomography for high-resolution monitoring of atmospheric water vapor over the Lisbon metropolitan area. It specifically assesses the feasibility of using a dense urban GNSS network, including low-cost receivers, to reconstruct the three-dimensional distribution of water vapor and evaluate its usefulness for short-term precipitation monitoring and nowcasting. The research investigates how station densification and observation geometry influence the quality of the tomographic inversion and the resulting water vapor fields. It also examines how GNSS-derived tomographic products can capture pre-convective moisture structures associated with rainfall events near Lisbon and its main airport. To achieve these objectives, a dense network of low-cost GNSS receivers was deployed across the Lisbon metropolitan area to complement the existing continuous-operating GNSS reference station network [31]. This combined setup aims to enhance the spatial density and geometric diversity of GNSS observations within an urban environment. To evaluate the accuracy and physical consistency of the tomographic results, independent vertical profiles of atmospheric water vapor from the meteorological station at Lisbon Airport serve as reference data. This study presents the first comprehensive evaluation of GNSS water vapor tomography in the Lisbon metropolitan area, using a hybrid network that combines low-cost receivers with a permanent

GNSS infrastructure, and explores its potential to provide quasi-real-time water vapor for urban-scale precipitation monitoring and nowcasting.

The study is organized as follows: Section 2 describes the study area, the GNSS dataset, the processing strategy, the tomographic algorithm, the overall modeling setup, and the ERA5, WRF, and radiosonde datasets used for evaluation. Section 3 presents the results and Section 4 the discussion. Finally, Section 4 summarizes the main conclusions of the work.

2. Materials and Methods

2.1. Study Area

The study area covers the metropolitan Lisbon region (Figure 1), stretching from the western coast to the Tagus River estuary. Along the western edge, the Atlantic shoreline features cliffs and some beaches, from Cascais, east of Lisbon. Inland, the landscape transitions to low-altitude hills and valleys, mostly below 300 m. Monsanto Hill, near the city center, is one of the most prominent landforms locally. To the north and northwest, the terrain becomes more rugged, culminating in the Sintra mountain range, which exceeds 500 m and is the region's highest feature. The Tagus River estuary dominates the southern and southeastern parts, forming a large, flat alluvial plain that significantly influences local weather patterns. Lisbon has a Mediterranean climate with strong Atlantic influences. Winters are generally mild and rainy, with most annual rainfall occurring from October/November to March/April. Heavy rainfall events are often associated with Atlantic frontal systems and low-pressure systems affecting the Iberian Peninsula. Summers are typically warm and dry.

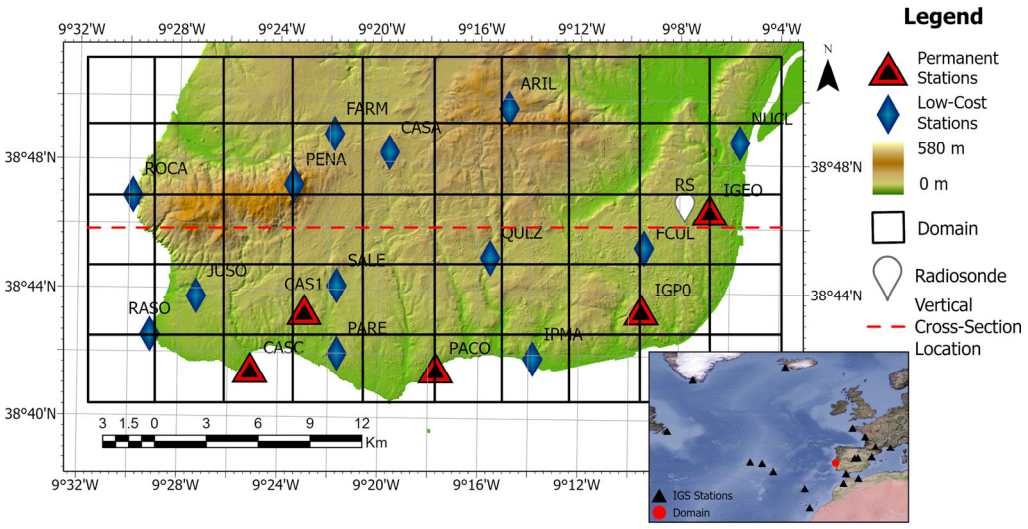


Figure 1. Distribution of the permanent and low-cost stations (shown as red triangles and blue diamonds, respectively) and the available radiosonde (white balloon) in the study area for performing GNSS tomography. The domain is outlined with black lines, and the red dashed line indicates where the vertical cross-section was created. The map in the lower-right corner shows all IGS network stations used in the GAMIT/GLOBK processing and the geographic location of the study area.

The observation campaign took place from August to December 2022. This study focuses on December, a period characterized by several intense storm events, especially early in the month, and has the most comprehensive data available. The experiment includes 18 continuously operating GNSS stations. Five are permanent stations belonging to the RENEP (National Network of Permanent Stations) and SERVIR (Virtual GNSS Reference Station System) networks. The remaining 13 are low-cost stations installed under the project EXPL/CTA-MET/0671/2021. Figure 1 shows the geographic distribution of

the GNSS stations. The CASC station is part of the EUREF (European Reference Frame) Permanent GNSS Network, while the IGEO station belongs to the SERVIR network.

2.2. GNSS Receivers and Antennas

The low-cost GNSS observation system used in this study features the Septentrio Mosaic-X5 receiver (firmware v4.14.10) and the u-blox ANN-MB series active antenna (ANN-MB-00). The Mosaic-X5 is a compact, multi-constellation, multi-frequency GNSS receiver module capable of tracking signals from major GNSS systems with an update rate up to 100 Hz. Its low power usage and small size make it suitable for embedded and high-dynamics applications. Additionally, it includes advanced RF interference mitigation technologies, such as anti-jamming and anti-spoofing features, which improve robustness in difficult environments (https://www.septentrio.com/en/products/gnss-receivers/gnss-receiver-modules/mosaic-x5, accessed on 15 January 2026).

The ANN-MB series is a multi-band active GNSS antenna supporting L1/L2/E5b/B2I frequencies and is compatible with GPS, GLONASS, Galileo, and BeiDou constellations. Its compact design, coupled with straightforward mounting options and versatile connectors, facilitates easy integration into high-precision GNSS configurations. The antenna is engineered to ensure reliable signal reception across multiple bands, thereby improving positioning accuracy and overall system performance (https://www.u-blox.com/en/product/ann-mb-series, accessed on 15 January 2026).

Before deployment, the performance of the low-cost GNSS system for PWV retrieval was evaluated against co-located geodetic-grade instruments, confirming its suitability for atmospheric applications; these results are beyond the scope of this study, as the main focus is on the tomographic framework and its performance, and several previous studies have already demonstrated the capability of similar low-cost GNSS systems for tropospheric sensing [20–29].

The remaining geodetic-grade receivers used in this study include the Leica GR30 (Leica Geosystems, St. Gallen, Switzerland), Trimble Alloy (Trimble Geospatial, Dubai, UAE), Trimble NetR9, Trimble NetR5, and Septentrio PolaRx5 (Septentrio, Leuven, Belgium), paired with antennas Leica LEIAR10, Trimble TRM57971.00, Trimble TRM159900.00, Trimble TRM55971.00, and Tallysman TWIVP6050_CONE.

2.3. GNSS Data Processing

The GNSS observations collected during the experiment were processed using the GAMIT/GLOBK (GG) package (version 10.71). The primary configuration settings used in the GG software are detailed in Table 1. This setup has been applied in multiple tomographic studies, including those by Benevides [10], Miranda, and Mateus [11], demonstrating its reliable performance in the Lisbon region. It was also extensively tested against alternative configurations, confirming their robustness and suitability for the analyses performed. Major limitations of low-cost GNSS are associated with Phase Center Variation (PCV) corrections that are often unknown, making them more vulnerable to errors such as multipath. To mitigate these errors, the U-blox ANN-MB-00 patch antenna used in this study was employed with a circular ground plane beneath the antenna to prevent the reception of reflected signals. This antenna includes a relative calibration proposed by Krietemeyer et al. (2020) [27] and available in the GG package used. Although they are less accurate than geodetic equipment, low-cost GNSS devices from various brands generally yield similar results. They are still suitable for integration into various geodetic tasks and can help increase the density of high-quality geodetic GNSS stations used to monitor tropospheric delay.

Table 1. Specific processing strategies used in GG software.

Parameter Name	Parameter Definition
Approach	DD (Double Difference)
Choice of observables	LC (Linear Combination of L1 and L2)
Cut angle	5°
Sampling interval	30 s
A priori dry air model	SAAS (Saastamoinen Model)
Dry and wet air mapping function	VMF3
Ocean tide model	FES2004
Solid tide model	IERS10
Clock and orbit	Final Product of the IGS
Satellite and antenna phase center	File IGS14 ANTEX
Tropospheric gradient estimation	2 h
Tropospheric Delay	Random walk with noise processing with 0.02 m$\sqrt{h}$
Ionospheric Effect	1 order (LC), 2 and 3 order correction

One disadvantage of GG software is the need to process each constellation individually, which takes longer than processing all constellations simultaneously. Another issue is the discontinuity in the daily time series of precipitable water caused by the stochastic parameter-estimation method, resulting in a divergence of several millimeters. To fix this, a time-window overlap strategy was implemented, where processing begins 6 h before (on the previous day, doy − 1) and continues 6 h after (on the next day, doy + 1), resulting in 36 h runs. The final water vapor time series is then generated by removing the first 6 and last 6 h of each run.

The accuracy of the GAMIT-derived ZTD was assessed against the IGS tropospheric products (TRO files), resulting in a mean bias of 2.1 mm, an RMSE of 8.4 mm, and a correlation of 0.97. It is important to note that a cutoff elevation angle of 5° was used in the GAMIT processing, whereas the IGS products are usually generated with a 7° cutoff, which may explain some minor differences between the solutions.

2.4. GNSS Tomographic Data and Setup

An unconstrained algorithm introduced by Miranda and Mateus [11], later refined by them, was used here to process GNSS tomography. The initial tomographic step involves creating a three-dimensional grid over the study area, which is a rectangular domain of 40×20 km^2 with 10 voxels in the east–west direction and 5 in the south–north direction. It has a horizontal resolution of 4 km and a variable vertical resolution, ranging from 500 m at the lowest levels to 1000 m at the highest levels. The adopted vertical and horizontal resolutions strike a balance between capturing spatial detail and maintaining inversion stability. A finer vertical resolution of 500 m is used in the lower troposphere to improve detection of water vapour variability while ensuring adequate ray coverage, especially given local topography. Conversely, a coarser resolution of 1000 m is applied at higher altitudes. Similarly, the 4 km horizontal resolution was chosen to balance spatial representativeness with the need to maintain a well-conditioned system. Terrain-following vertical spacing was employed, allowing the levels to follow the terrain's altitude. This approach offers advantages over the traditional method (voxels at a single altitude) because it positions the voxels so that stations are roughly at their base, reducing the need for altitude corrections in the base voxels.

To address the ill-posed problem inherent in GNSS tomography, which arises from a lack of observations (GNSS signals), particularly in surface voxels, observed signals are used to generate virtual observations. The equation proposed by Miranda and Mateus [11] uses real observations and the least squares method to obtain coefficients for an optimal fit

of a hypersurface that allows virtual rays to be generated at any elevation and azimuth. It is given by:

$$SIWV_{i,k} = a_i \cos(\alpha_{i,k}) + b_i \sin(\alpha_{i,k}) + \frac{c_i}{\sin(\varepsilon_{i,k})} + d_i (i = 1, \ldots, n; k = 1, \ldots, N) \quad (1)$$

where $SIWV_{i,k}$ represents the slant observations at the stations i, where k is an observation, $\alpha_{i,k}$ and $\varepsilon_{i,k}$ are, respectively, the azimuth and elevation; n and N correspond to the number of stations and the number of rays in the defined time windows. a_i, b_i, c_i and d_i are coefficients to be estimated. The time window was set to 1 h, i.e., all observations recorded within this period are used to estimate the coefficients. Applying this equation, which yields virtual rays throughout the domain, i.e., all voxels have a minimum number of rays (equal to the number of stations) that intersect them, enables a 100% matrix rank.

The equation used for parameter adjustment is given by:

$$SIWV_j = a_i \cos(\alpha_j) + b_i \sin(\alpha_j) + \frac{c_i}{\sin(\varepsilon_j)} + d_i (j = 1, \ldots, J) \quad (2)$$

where J is the number of target voxels. To include the rays within the tomographic domain that enter the domain from the lateral boundaries, the observed $SIWV_j$ must be corrected to disregard the impact of the water vapor on the signal outside the domain.

The equation used for this purpose is proposed by Miranda et al. [32], which is an improved version of the equation by Miranda and Mateus [11]:

$$SIWV_j^{'} = SIWV_j \cdot e^{-z/H_v} \quad (3)$$

where $SIWV_j^{'}$ is the observation corrected, z is the altitude at which the rays enter the domain and H_v is the scale height of water vapor. This formulation assumes that the atmosphere outside the domain decreases exponentially in water vapor density. Miranda et al. [32] concluded that keeping H_v constant (usually at 2000 m, [33]) degrades the tomographic result, as H_v exhibits daily and seasonal cycles that influence the tomographic solution.

H_v can be estimated according to the following formulation:

$$H_v = \frac{PWV}{\rho_{vs}} \quad (4)$$

where ρ_{vs} is the ρ_v at the surface (in kg/m^3) [34]. Equation (4) is applied independently to each station, enabling the representation of spatial variability in H_v. A limitation of this strategy is that ρ_{vs} must be derived from external datasets, such as numerical weather models, radiosonde measurements, or meteorological stations. This requirement introduces external constraints, rendering the algorithm proposed by Miranda and Mateus [11] no longer fully unconstrained and unable to operate in real time, since it depends on external data that is typically unavailable in real time. In the present study, ERA5 reanalysis data are used to estimate the ρ_{vs} field, which is then bilinearly interpolated to each GNSS station location.

2.5. ERA5 Dataset

The ERA5 model, developed by the Copernicus Climate Change Service (C3S) at the European Center for Medium-Range Weather Forecasts (ECMWF), is the fifth generation of atmospheric reanalysis from this center. It spans from January 1940 to the present, with a temporal resolution of 1 h and a spatial resolution of about 30 km. Data are available at 37 pressure levels, ranging from 1000 to 1 hPa. Despite certain limitations and biases, ERA5

remains the best available alternative when observational data are missing. It incorporates many more observations, increasing from an average of 0.75 million per day in 1979 to over 24 million in recent years. This growth is mainly due to improved satellite observations and new data sources, including GNSS-RO, satellite radiances, ocean wind fields, ozone products, and in situ observations [35].

The density of water vapor (ρ_v in kg/kg) is not directly available in the ERA5 dataset, but can be calculated using the atmospheric pressure (P, in Pa), the specific humidity (q, in kg/kg), and the virtual temperature (T_v, in K) by:

$$\rho_v = \frac{P \cdot q}{287.055 \cdot T_v}, \quad (5)$$

where T_v (K) is given by:

$$T_v = T \cdot (1 + 0.61 \cdot q), \quad (6)$$

where T (K) is the air temperature [36]. Additionally, bilinear interpolation was applied to all variables, in which the value at a given location is estimated from the four nearest grid points, weighted by their relative distances.

2.6. WRF Model

The Weather Research & Forecasting Model (WRF) version 4.3 [37] was used to generate weather data at high vertical and horizontal resolution, thereby improving the ERA5 model's resolution. Two domains were configured to achieve these resolutions. The primary domain, centered on Portugal, has a grid spacing of 12 × 12 km and covers an area of 4,416,192 km^2 (1968 km east–west and 2244 km north–south). This domain encompasses the entire Portuguese territory, avoiding discontinuity problems at its edges. The nested domain has a grid spacing of 4 × 4 km, covering an area of 612,864 km^2 (912 km east–west and 672 km north–south). Both domains have 70 vertical levels, from the surface to approximately 30 km altitude (fixed at 10 hPa). The main physical options selected included the WRF single Moment 6-class microphysical scheme [38], the Mellor-Yamada-Janjic scheme for the planetary boundary layer [39], the Rapid Radiative Transfer Model scheme for shortwave and longwave radiation [40], the Betts-Miller-Janjic scheme for cumulus parameterization [39], and the National Centers for Environmental Prediction (NCEP), Oregon State University, Air Force and Hydrology Laboratory land surface model for land surface parameterization [41]. The initial and lateral boundary conditions used in the parent domain are derived from ERA5 data. The WRF model does not simulate directly the ρ_v, but it can be calculated using the following formulation:

$$\rho_v = \frac{e}{461.51 \cdot T}, \quad (7)$$

where e is the partial pressure of water vapor (Pa), given by:

$$e = \frac{r \cdot P}{0.622 + r} \quad (8)$$

where r is the water vapor mixing ratio (kg/kg) [36].

2.7. Radiosonde Data

A total of 32 radiosonde profiles launched in December 2022 were used to evaluate the tomographic solutions for that month. Data were acquired by the radiosonde (Vaisala RS92-SGP), which is launched daily at approximately 11:15 UTC from an altitude of 105 m at the Portuguese Institute for Sea and Atmosphere center (Φ = 38.77, λ = −9.12), located within the tomography domain. The radiosonde directly measures the water vapor mixing ratio (r);

thus, the water vapor density can be derived using Equations (7) and (8). As the radiosonde ascends, its geographic position is estimated [42], and the corresponding tomographic voxel containing the probe at each time step is identified. The water vapor density within that voxel is then extracted and compared with the radiosonde-derived measurements.

3. Results

This section presents the results of GNSS tomographic reconstructions in the Lisbon metropolitan area, highlighting how network densification and setup influence the quality of three-dimensional atmospheric water vapor fields. Consistent with the study's goals, three experimental scenarios were designed: (i) a hybrid setup combining permanent and low-cost GNSS stations (TOMO_PL); (ii) a configuration using only low-cost stations (TOMO_L); (iii) a setup based solely on permanent stations (TOMO_P). The purpose of this design is to systematically assess how increasing network density by adding low-cost receivers affects the conditions of the tomographic inversion and the resulting spatial distribution of water vapor.

The performance of each configuration is assessed through both quantitative and qualitative analyses. Quantitatively, the reconstructed three-dimensional water vapor density fields are compared with independent reference datasets, including outputs from the Weather Research and Forecasting (WRF) model, the ERA5 reanalysis, and radiosonde (RS) observations. Qualitatively, the spatial and vertical structures of the tomographic solutions are examined to evaluate their consistency and ability to represent atmospheric variability over the Lisbon region.

The following analysis concentrates on December 2022, a month marked by several precipitation events, including a severe storm that impacted the Lisbon metropolitan area. These weather conditions provide a useful case for assessing the performance of GNSS tomographic reconstructions under changing, moisture-rich atmospheric conditions. The average vertical profiles of water vapor density from the three tomographic configurations (TOMO_PL, TOMO_L, and TOMO_P), along with those from WRF, ERA5, and radiosonde observations, are shown in Figure 2a. All datasets display the expected quasi-exponential decline in water vapor density with altitude, with maximum values around 10 g m^{-3} at the surface and decreasing gradually to near zero at about 8 km. This vertical profile aligns with typical winter atmospheric conditions over the Lisbon area.

In the lower troposphere (from the surface up to about 2.5 km), the tomographic solutions consistently underestimate water vapor density compared to the reference datasets. Above this layer, a slight overestimation is observed across all three configurations (see Figure 2c). The vertical distribution of the root-mean-square error (RMSE), shown in Figure 2b, indicates that errors remain below 2 g m^{-3} at all altitudes and for all configurations. Among them, TOMO_P exhibits the largest RMSE values, as expected, since this setup depends solely on five permanent GNSS stations, most of which are in the southern part of the domain near the Tagus estuary. Such a sparse, uneven spatial setup weakens the inversion's conditioning and limits the ability to accurately reconstruct the data.

The configurations using low-cost receivers (TOMO_PL and TOMO_L) show improved performance, with TOMO_PL slightly outperforming, particularly compared to ERA5 (see Figure 2). This improvement highlights the positive effect of higher network density on the robustness and spatial representativeness of the tomographic inversion. However, discrepancies between WRF and radiosonde profiles indicate that numerical weather prediction outputs and in situ soundings, which provide atmospheric information particularly at finer vertical resolution, are not fully captured by the tomographic system.

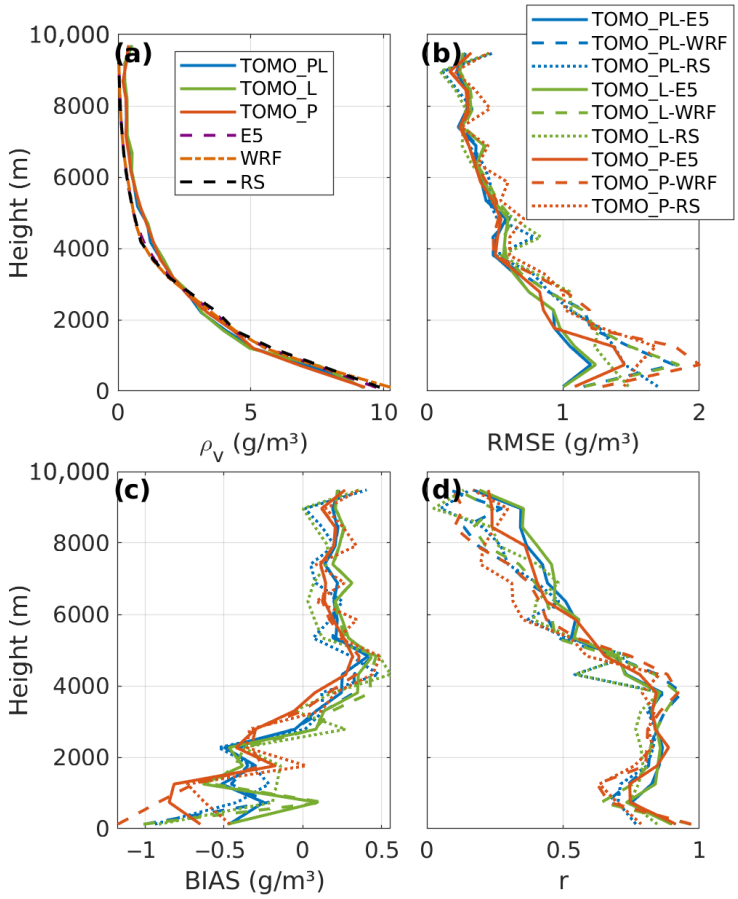


Figure 2. Vertical assessment of the three tomography solutions. (**a**) Average of all vertical profiles of December 2022 (at RS geographic location, see Figure 1); (**b**) the RMSE of all solutions versus the ERA5 (E5 in legend), the WRF, and RS data; (**c**) the BIAS; (**d**) the correlation (*r*).

The vertical distribution of the Pearson correlation coefficient (r), shown in Figure 2d, further supports these findings. Between the surface and about 4 km altitude, correlation values are near 0.8, indicating strong agreement among the tomographic solutions and the reference datasets within the lower and middle troposphere. Above this level, the correlation gradually drops, reaching roughly 0.5 near 6 km and falling below 0.5 in the upper troposphere. These lower correlations at higher levels arise from the Pearson correlation coefficient's dependence on signal variance. In the upper troposphere, where ρ_v and its variability are very low, even small absolute differences can lead to relatively large fluctuations, reducing correlation. In contrast, the greater variability in the lower troposphere leads to stronger covariance and, consequently, higher correlation, despite larger absolute errors (higher RMSE).

To further assess the temporal consistency of the reconstructed fields during this highly active month, Figure 3 presents Hovmöller diagrams of water vapor density for the three tomographic configurations, along with ERA5, WRF, and radiosonde observations. Hovmöller diagrams provide a time–height perspective on atmospheric moisture changes, identifying temporal gradients, vertical moisture transport, and the persistence of humid or dry layers. A 12 h temporal resolution was used to align with the radiosonde launch times at 00:00 and 12:00 UTC.

Overall, the diagrams show a clear qualitative similarity among the tomographic solutions, the numerical models, and the radiosonde data. The main temporal patterns, including the alternation between moist and relatively dry periods, are consistently reproduced. In particular, TOMO_PL shows improved agreement with the reference datasets,

especially in the lower troposphere between days 10 and 15, December. During this period, a rise in near-surface moisture is detected and coincides with the extreme precipitation event reported during that time. The temporal gradients associated with this event are well captured, and the timing of moisture peaks and lows closely aligns with both the observed and modeled evolution.

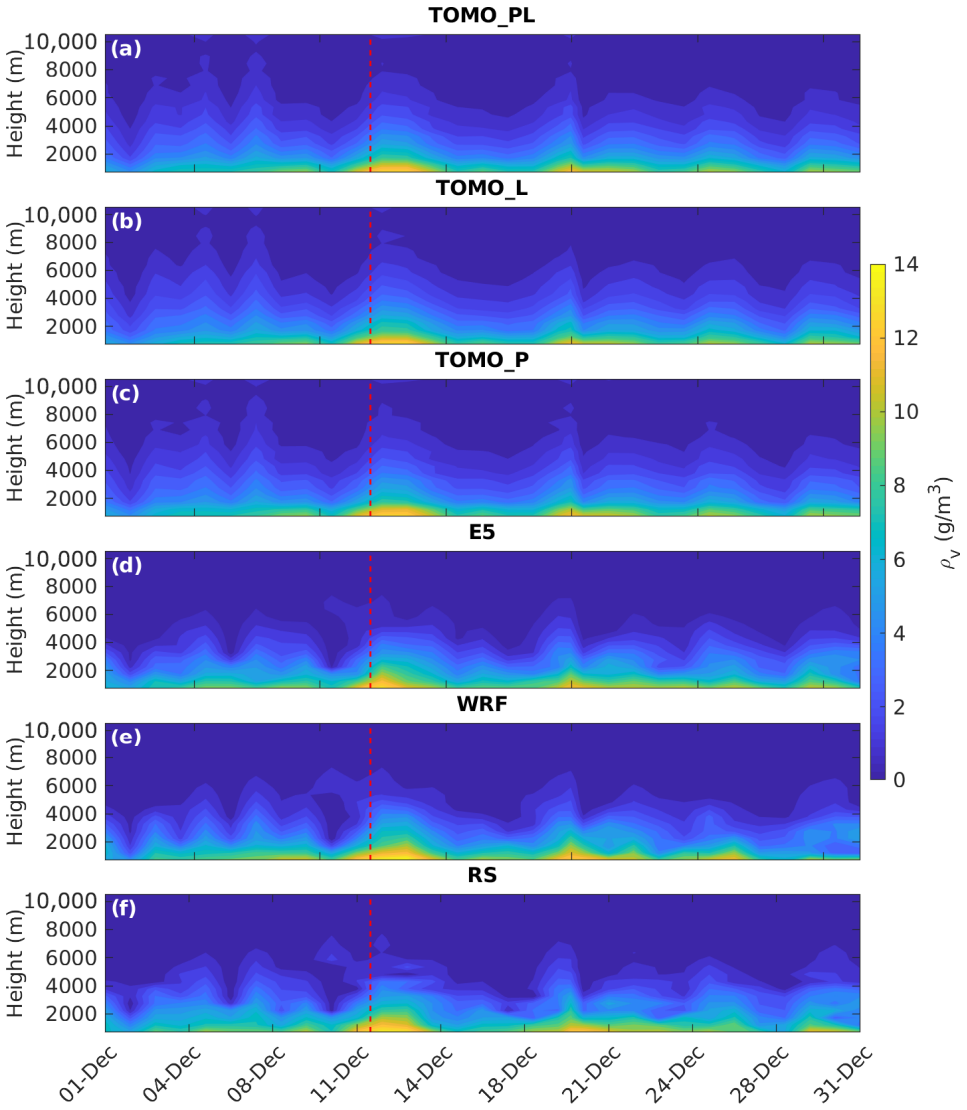


Figure 3. Hovmöller diagrams with a temporal resolution of 12 h, aligned to the RS launch times at 00 h and 12 h UTC. (**a**) TOMO_PL; (**b**) TOMO_L; (**c**) TOMO_P; (**d**) ERA5 (E5); (**e**) WRF; (**f**) RS. The vertical dashed red indicates the beginning of a precipitation extreme event and shows the position of the cross-section represented in Figure 4.

In line with the vertical profile analysis, all tomographic configurations tend to overestimate water vapor content at higher levels. However, the differences among TOMO_PL, TOMO_L, and TOMO_P are subtle in the Hovmöller representation, indicating their similar vertical structures. A significant limitation appears on 10 December, when a strong moisture intrusion around 6 km altitude, clearly shown in WRF, ERA5, and radiosonde profiles, is not captured by any of the tomographic solutions. This discrepancy emphasizes the inherent challenges of GNSS tomography in resolving localized and transient mid- to upper-tropospheric features, especially during conditions of intense vertical variability. Despite these challenges, the overall consistency of the tomographic reconstructions supports

their potential usefulness for operational atmospheric monitoring and as supplementary input for weather forecasting.

Between December 11 and 13, a severe precipitation event impacted the Lisbon metropolitan area, with rainfall exceeding 120 mm within 24 h. The event was associated with an organized convective system that produced intense, persistent rainfall, resulting in flash flooding in several urban areas. The high atmospheric moisture during this episode is clearly depicted in the time–height representation (Figure 3), where water vapor density in the lower troposphere (from the surface to about 2 km) approaches 14 g m^{-3}. This period, therefore, provides a rigorous test case for evaluating whether tomographic reconstructions accurately depict the vertical moisture profile under strong atmospheric forcing.

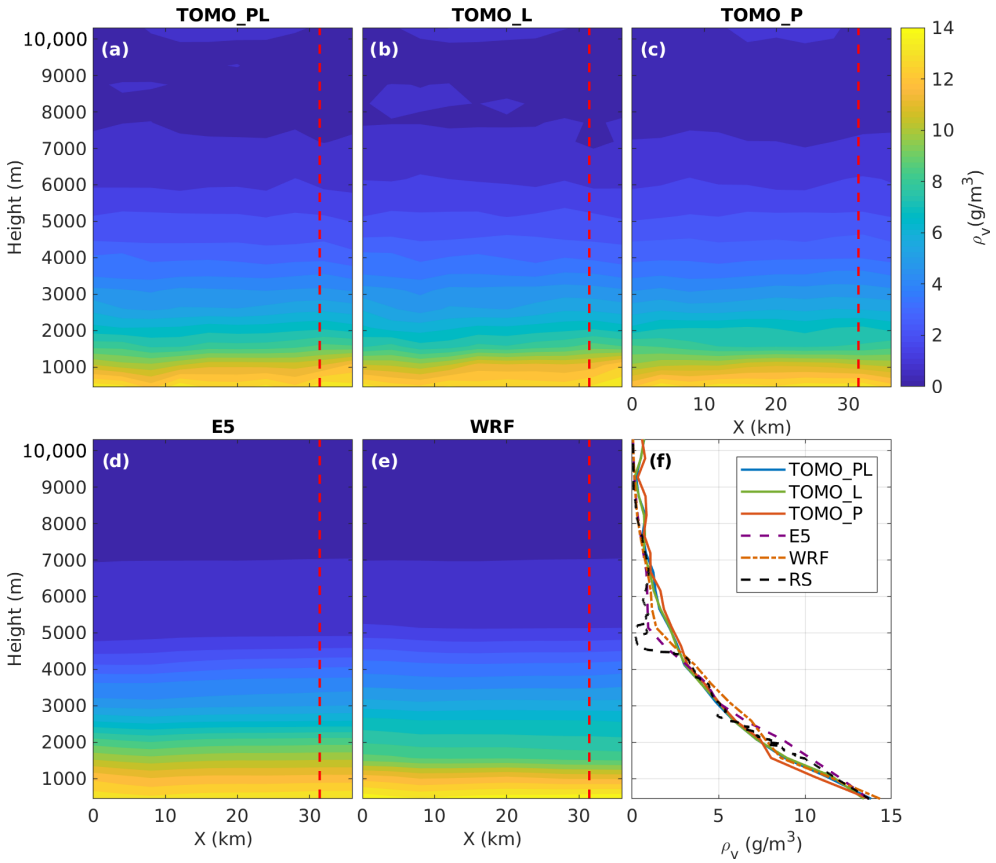


Figure 4. Water vapor density vertical cross-section (see the location on Figure 1, red dashed line) on day 12th at 00h UTC close to the beginning of a severe rainfall event in the Lisbon area: (**a**) TOMO_PL solution; (**b**) TOMO_L; (**c**) TOMO_P; (**d**) ERA5 model; (**e**) WRF; (**f**) the vertical profile of water vapor density at RS location for all products and the RS profile.

To further examine the ability of different products to resolve vertical variability during the start of the event, vertical cross-sections for 12 December at 00:00 UTC are shown in Figure 4a–e for the three tomographic configurations, ERA5, and WRF. This time marks the early stage of the extreme rainfall episode. The cross-section, oriented west–east and located near the radiosonde site (see the red dashed line in Figure 1), allows for a consistent comparison between the reconstructed fields and the in situ observations. Additionally, Figure 4f displays the vertical water vapor density (ρ_v) profile measured by the radiosonde at 00:00 UTC, along with the corresponding profiles extracted from TOMO, ERA5, and WRF at the radiosonde location.

Visually, tomographic solutions and numerical models mostly share similar vertical structures. From the surface up to about 4.5 km altitude, the magnitude and vertical gradients of water vapor density are consistent across all datasets. However, differences become

more noticeable in the upper troposphere (>4.5 km). The tomographic solutions show increased variability and retain significant moisture near the top of the domain, likely due to weaker observational constraints and less ray-path coverage at higher altitudes. As previously discussed, this behavior aligns with GNSS tomography's tendency to overestimate moisture in the upper layers.

Systematic differences are also seen between ERA5 and WRF. ERA5 shows a smoother, more vertically spread moisture profile within the first 2 km due to its coarser vertical resolution and strong data assimilation constraints. In contrast, WRF displays a more concentrated moisture layer near the surface, a feature also captured by the tomographic reconstructions. At the radiosonde location (Figure 4f), ERA5 closely matches the observed profile from the surface up to about 4.5 km; however, this agreement should be viewed with caution since ERA5 assimilates radiosonde data. The tomographic solutions align well with both WRF and the radiosonde in the lowest 2 km, indicating that the dense GNSS setup can effectively capture near-surface moisture variability during heavy precipitation events.

Notably, the radiosonde profile shows a relatively dry layer around 5 km in altitude, which neither the tomographic reconstructions nor the numerical models detect. This discrepancy emphasizes the difficulty of identifying localized mid-tropospheric dry intrusions using GNSS tomography, especially when the inversion's vertical resolution is limited and the signal contribution from higher layers is weak. Overall, while the tomographic system performs well in the lower troposphere during this extreme event, it still struggles to accurately capture fine-scale vertical structures and variability at upper levels.

An analysis of the average spatial variability of precipitable water vapor (PWV) is shown in Figure 5. PWV was first calculated for each product by vertically summing the water vapor density fields, then averaged over the entire study period to create a representative spatial PWV pattern for each dataset. This column-integrated measurement is especially useful for assessing the potential of GNSS-derived humidity fields to support weather forecasting, as it decreases sensitivity to small-scale vertical mismatches while maintaining the main spatial gradients of atmospheric moisture.

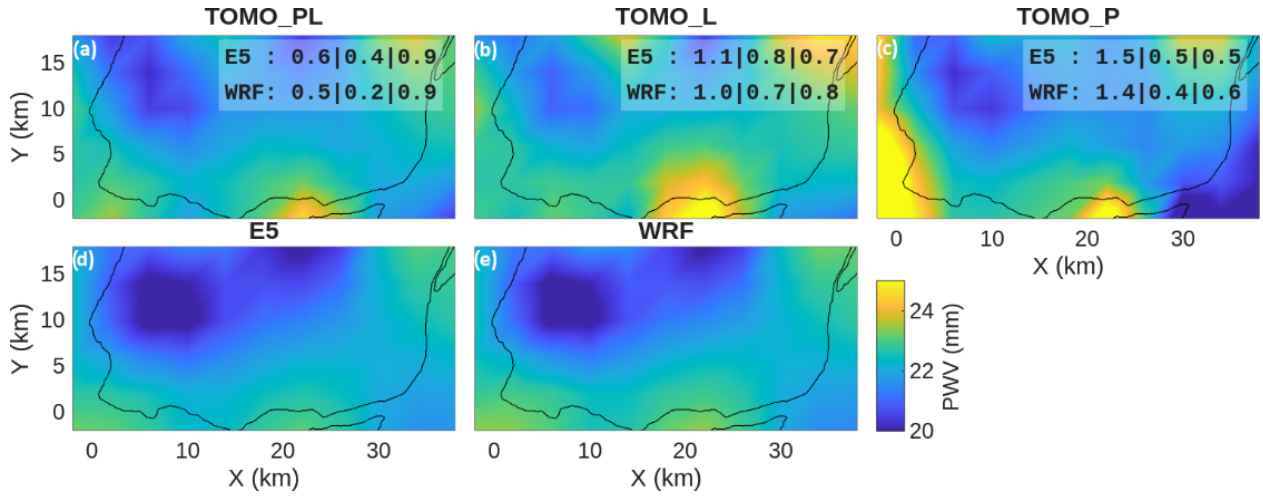


Figure 5. Mean PWV, calculated from all PWV maps during the time span: (**a**) for the TOMO_PL solution; (**b**) TOMO_L; (**c**) TOMO_P; (**d**) using the ERA5 model data; (**e**) WRF. The first line in the table (**a**–**c**) shows the RMSE, bias, and Pearson correlation, respectively, against ERA5, the second line against the WRF. A positive bias indicates a TOMO overestimation of ρ_v. The black line in all plots refers to the coastline.

The close agreement between ERA5 and WRF is expected because ERA5 was used to initialize the WRF simulations. Additionally, voxelization performed before the com-

parison further aligns spatial sampling and effective resolution, thereby reducing structural differences between the two model-based products and producing more consistent PWV patterns.

The spatial PWV field shows a clear minimum over the highest terrain in the area, which is the Sintra mountain range (x ≈ 8 km, y ≈ 12 km; elevation ~510 m). This topographic feature acts as an orographic barrier to moist onshore flow, limiting moisture advection toward the northern part of the study area. The lower PWV values north of the domain are thus physically consistent with the prevailing maritime influence and the local terrain's effect on moisture transport, serving as a useful benchmark for assessing whether the tomographic products accurately depict meteorologically plausible spatial patterns.

Among the tomographic configurations, TOMO_PL best matches the model-based PWV patterns, with a spatial RMSE of 0.6 g m^{-3}, a positive bias of 0.4 g m^{-3} (indicating a slight overestimate), and a high spatial correlation of 0.9. This supports the idea that increasing network density by adding low-cost receivers improves inversion conditioning and yields a more realistic reconstructed moisture distribution. In contrast, TOMO_P provides the least reliable PWV field, with a much larger RMSE of 1.5 g m^{-3} and weak spatial correlations of 0.5 and 0.6 with ERA5 and WRF, respectively. These problems stem from the limited number of stations and their uneven spatial distribution, which limit ray-path coverage and reduce sensitivity to actual horizontal gradients.

A clear sign of these limitations is the west–east imbalance in TOMO_P: the solution tends to overestimate moisture in the western part of the domain, especially over the ocean, while underestimating PWV in the eastern part of the domain over the Tagus estuary. Since there is no independent evidence supporting such a persistent dipole structure, this pattern is more likely to be caused by inversion artifacts due to insufficient geometric constraints rather than by actual atmospheric variability. Importantly, these artifacts can produce false gradients that resemble mesoscale signals, underscoring the need for dense, evenly distributed GNSS deployments when tomographic products are used for meteorological interpretation or data assimilation.

A complementary categorical validation of the tomographic products is shown in Figure 6 using a pooled contingency table analysis against ERA5 and WRF. PWV fields were classified into five moisture categories based on empirical quantiles (0, 0.2, 0.4, 0.6, 0.8, 1): very low (VL), low (L), moderate (M), high (H), and very high (VH). This method is intentionally strict: by assessing class membership rather than continuous values, it uncovers systematic biases in the reconstructed moisture distribution and indicates whether the tomography accurately captures atmospheric humidity regimes under different conditions. Commission error refers to the proportion of cases incorrectly assigned to a class, while omission error is the proportion of cases in that class that the method fails to identify.

Across both references (ERA5 in Figure 6a–c and WRF in Figure 6d–f), a consistent pattern emerges. TOMO_PL shows its strongest agreement at the class level in the high-moisture regime, correctly reproducing 19.21% of ERA5 "High" cases, with limited leakage to neighboring classes (0.66% to Moderate; 0.77% to Very High). The second-highest diagonal contribution occurs for the Very High class (16.94%), indicating that TOMO_PL reliably detects intense moisture episodes but tends to compress extremes into adjacent categories, thereby reducing spatial–temporal contrast. The Moderate class, while not having the highest diagonal value, dominates the contingency matrices because it is common in both datasets. The clustering of tomographic outcomes around this class aligns with the well-known smoothing behavior of GNSS tomography when inversion is weakly constrained or when ray coverage is insufficient to resolve sharp gradients. This limitation, especially relevant in highly dynamic layers, has been repeatedly noted in the tomography literature

as a consequence of geometry, regularization, and the ill-posed nature of the reconstruction problem [14,43].

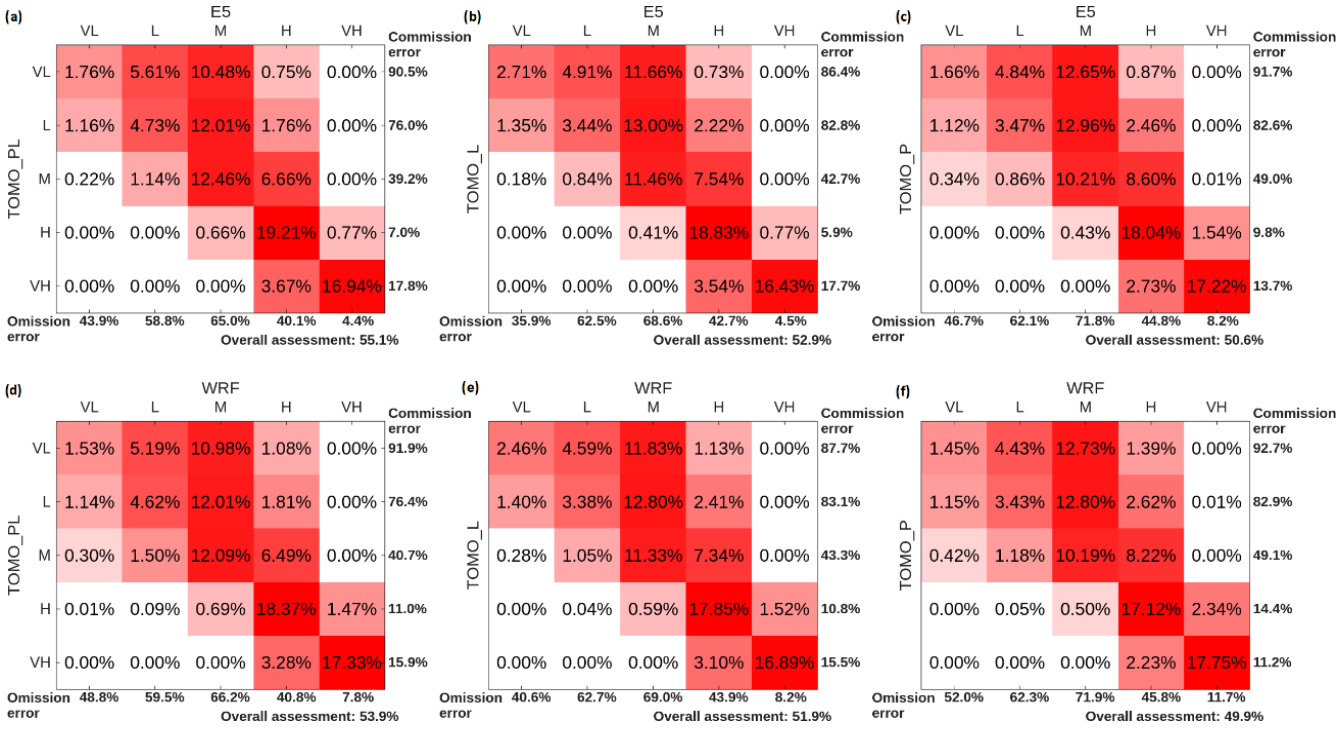


Figure 6. Contingent tables between the tomographic solutions, ERA5, and WRF in a "pull-together mode" and considering five classes based on the quartiles 0, 0.2, 0.4, 0.6, 0.8, and 1, named very low (VL), low (L), moderate (M), high (H), and very high (VH): (**a**) TOMO_PL vs. ERA5; (**b**) TOMO_L vs. ERA5; (**c**) TOMO_P vs. ERA5; (**d**) TOMO_PL vs. WRF; (**e**) TOMO_L vs. WRF; (**f**) TOMO_P vs. WRF.

In contrast, the dry-air regimes are poorly represented: VL and L show very high commission errors (90.5% and 76.0%, respectively), indicating that TOMO_PL rarely produces genuinely low-moisture states. This is not just a statistical artifact of quantile binning; instead, it highlights a physical–methodological sensitivity gap. GNSS slant delays integrate refractivity along ray paths and are therefore less sensitive to small changes in absolute humidity, whereas regularization and limited vertical information further reduce the detection of dry intrusions and sharp moisture discontinuities. As a result, the system tends to revert to intermediate humidity values, increasing Moderate classifications at the expense of VL/L detection. Similar patterns, better accuracy in moist conditions but decreased sensitivity in dry conditions, have also been observed in GNSS-based humidity products and in their evaluations against reanalysis and radiosondes [1].

The comparative ranking of the three configurations also matches the continuous metric results shown earlier. TOMO_L and TOMO_P generally produce the same regime-dependent behavior, with peak agreement again concentrated in H and VH. TOMO_L slightly surpasses in detecting intense moisture (18.83% and 16.43%), while TOMO_P tends to smooth values into the Moderate class (up to 12.96%) and has higher commission errors in dry categories, consistent with lower geometric strength. The overall accuracy metrics (55.1% for TOMO_PL, 52.9% for TOMO_L, and 50.6% for TOMO_P against ERA5; and 53.9% for TOMO_PL against WRF, exceeding TOMO_L and TOMO_P by about 2% and 4%) confirm that densification, especially when combining permanent and low-cost stations, enhances the categorical accuracy of the moisture field.

From a broader perspective, these findings align with previous research indicating that reconstruction quality is heavily influenced by network geometry, observation density,

and inverse-problem conditioning. Furthermore, densification using low-cost receivers can improve meteorological usefulness when data quality is sufficient [44]. Therefore, while TOMO_PL clearly aids in detecting and monitoring elevated moisture conditions relevant to heavy-precipitation forecasts, its current setup may require additional constraints, such as adaptive regularization, flow-dependent background fields, or multi-sensor integration, to better distinguish low-humidity states and preserve extreme gradients.

4. Discussion

This study assessed the performance of GNSS water-vapor tomography across the Lisbon metropolitan area, considering network density and composition, focusing on December 2022, a period marked by multiple rainfall events and a major storm affecting a densely populated urban region. The results demonstrate that increasing observation density by adding low-cost GNSS receivers significantly improves the realism, consistency, and practical usefulness of the reconstructed three-dimensional moisture fields. These benefits are especially evident in the lower troposphere and in the column-integrated moisture signal (PWV), both of which are directly relevant to short-term precipitation forecasting and impact-based warnings in urban environments.

A consistent finding across all diagnostics is that densified configurations outperform the sparse permanent-only setup. The hybrid configuration, which combines permanent and low-cost stations (TOMO_PL), generally provides the most balanced solution: it reduces inversion artifacts, improves spatial coherence, and more accurately captures the temporal evolution of near-surface moisture during December 11–13. The low-cost-only dense configuration (TOMO_L) shows a similar overall behavior, indicating that network density is a key factor in improvement, while adding permanent stations provides additional stability and small gains relative to reference datasets.

The added benefit of densification is especially evident when analyzing spatial patterns of PWV. Densified solutions produce physically plausible spatial gradients that align with local topographic effects, such as lower PWV over the Sintra mountain range and a moisturizing shadow north of the orographic barrier. In contrast, the sparse permanent-only solution (TOMO_P) shows spatial inconsistencies, with overestimations in the western area, particularly offshore, and underestimations in the eastern part near the Tagus estuary. These dipole-like patterns are unlikely to be persistent atmospheric features and are better understood as inversion artifacts arising from weak geometric constraints and an uneven station distribution. This is crucial for operational use: false gradients can mimic mesoscale moisture convergence, leading to misleading interpretations during high-impact weather events. Therefore, densification not only improves the accuracy metrics but also enhances the reliability of the product as a meaningful meteorological field.

Despite these improvements, the analyses still reveal limitations under dense network conditions. First, all tomographic solutions tend to underestimate moisture in the lower layers and overestimate it at higher levels, with a decreasing correlation above mid-tropospheric altitudes. The time–height diagnostics show that, although temporal gradients are generally well captured in the lower troposphere, some mid-level intrusions observed in radiosonde data and reflected in the models (e.g., moisture anomalies around 6 km) are not reproduced by any tomographic setup. Likewise, comparisons of vertical cross-sections at the onset of the extreme rainfall event suggest that tomography can accurately represent the moist boundary layer but struggles to capture small-scale structures in the mid-troposphere, such as dry layers or abrupt humidity changes. These issues are consistent with the ill-posed nature of GNSS tomography, the limited information content of slant delays at higher altitudes, and the smoothing effects introduced by regularization and discretization. In practice, tomography appears most reliable for diagnosing low-level

moistening and column water vapor, while its ability to depict upper-level humidity and sharp vertical contrasts remains less reliable.

The categorical verification further clarifies the strengths and weaknesses of the tomographic products. Agreement is highest in high- and very-high-moisture regimes, indicating that the system can detect moisture-rich conditions associated with heavy precipitation events; however, it often underestimates the extremes (i.e., it tends to compress the most extreme values). Conversely, performance is poor in very low and low moisture classes, reflecting limited sensitivity to dry-air conditions and a bias toward mid-range values. This behavior aligns with the smoothing tendency observed in continuous comparisons and suggests that the most immediate meteorological value lies in monitoring moisture buildup and persistence, rather than diagnosing dry intrusions or strongly layered humidity profiles.

These findings largely align with previous GNSS tomography studies that identify network geometry as a key factor influencing reconstruction quality (e.g., [45–47]). They also show that performance is usually strongest in the lower troposphere, while retrievals at higher levels remain difficult (e.g., [48–50]). The current results build on this knowledge by demonstrating that low-cost densification can provide real benefits in a coastal urban area where rainfall forecasting is crucial. However, the remaining limitations imply that densification alone cannot fully solve the fundamental challenges of GNSS tomography. Improving the representation of sharp vertical gradients and mid-level dry intrusions probably requires methodological advances, such as flow-dependent or background-field constraints, adaptive regularization, better voxel design, and comprehensive observation-quality screening to reduce coastal multipath and site-specific biases [11,51].

From a forecasting perspective, the results support two complementary methods for use in urban and densely populated areas. First, dense GNSS tomography can serve as a near-real-time monitoring tool to detect low-level moisture surges and their development, which are key precursors to heavy rainfall and flash floods [2,52,53]. Second, tomographic products can enhance numerical weather prediction systems, especially at high temporal resolution, by providing boundary-layer humidity constraints and PWV estimates [2]. However, to have a measurable impact on forecasts, assimilation strategies must address known error structures, such as altitude-dependent bias, smoothing, and limited dry-regime discrimination, and should target the conditions and layers where tomography demonstrates clear skill [54].

Despite the strengths of the approach, a limitation should be acknowledged: the virtual observations are derived from a fitted model based on GNSS-processed (i.e., mapped) observations rather than raw measurements (Equations (1)–(3)), which may introduce smoothing effects and reduce sensitivity, especially at low elevation angles (<5°). Additionally, the use of a priori information, such as the surface water vapor density (ρ_v) derived from ERA5, used here to determine the scale height (Hv), may further restrict the solution and affect the independence of the reconstruction. However, the overall consistency of the results indicates that these limitations do not substantially compromise the robustness of the tomographic retrieval; furthermore, the framework can function entirely independently when in situ meteorological observations are available within the tomographic domain, which is not the case in this study.

5. Conclusions

This work demonstrates that expanding a GNSS network with low-cost receivers improves the quality, coherence, and meteorological interpretability of water-vapor tomography across the Lisbon metropolitan area. The hybrid setup (TOMO_PL), which combines permanent and low-cost stations, consistently outperforms a sparse permanent-only system

and offers a small but reliable advantage over the low-cost-only configuration. The most significant improvements are seen in the lower troposphere and in PWV, where the reconstructed fields show stronger agreement with independent references and better capture moisture fluctuations during a high-impact rainfall event.

Quantitatively, the densified GNSS configuration outperformed the sparse permanent-only network across most evaluation metrics. In the vertical assessment, all tomography solutions kept RMSE values below 2 g m^{-3}, while correlations were strongest in the lower to middle troposphere, reaching about 0.8 below 4 km and decreasing to around 0.5 near 6 km. The hybrid configuration (TOMO_PL) provided the best overall PWV agreement, with a spatial RMSE of 0.6 g m^{-3}, bias of 0.4 g m^{-3}, and correlation of 0.9, whereas the sparse permanent-only setup (TOMO_P) showed much poorer performance, with RMSE up to 1.5 g m^{-3} and weaker spatial correlations (0.5–0.6). In the categorical validation, TOMO_PL also achieved the highest overall accuracy, reaching 55.1% against ERA5 and 53.9% against WRF, confirming that low-cost network densification substantially improves the retrieval of boundary-layer humidity and column-integrated moisture, particularly during high-moisture and heavy-rainfall conditions.

The results highlight four key conclusions. (1) Increasing network density significantly enhances the accuracy of tomographic inversion and better captures storm-related moisture signals, especially near the surface, which is vital for urban rainfall forecasts. (2) Sparse and unevenly distributed networks can create inversion artifacts that resemble real physical gradients, complicating interpretation during severe weather events. (3) Even with a dense network, GNSS tomography has inherent limitations, such as lower accuracy at higher levels, smoothing sharp vertical gradients, and reduced sensitivity to dry conditions and mid-tropospheric dry intrusions. These limitations are mainly related to the geometry of GNSS observations and the unconstrained nature of the inversion, and could potentially be mitigated by introducing additional horizontal and vertical constraints or multi-source data fusion. (4) The most effective way to improve forecasts is to utilize tomography, where it performs best—particularly for boundary-layer humidity and column water vapor—either for nowcasting or through data assimilation methods that explicitly account for product uncertainty and error variations with altitude.

Overall, the findings endorse using dense GNSS networks, including low-cost receivers, as a practical way to improve atmospheric moisture monitoring in urban areas. This is especially crucial for storm and flash-flood forecasting, where quick detection of low-level moisture buildup can enhance situational awareness and potentially improve short-term predictions. Future improvements will likely depend on combining denser grids with methodological advances that reduce smoothing, strengthen upper-level constraints, and better capture sharp humidity structures that influence convective development.

Author Contributions: Conceptualization, R.M., P.M. and J.C.; methodology, R.M. and P.M.; software, R.M.; validation, R.M., P.M. and J.C.; formal analysis, R.M., P.M. and J.C.; investigation, R.M.; resources, P.M.; data curation, R.M.; writing—original draft preparation, R.M.; writing—review and editing, R.M., P.M. and J.C.; visualization, R.M., P.M. and J.C.; supervision, P.M. and J.C.; project administration, P.M.; funding acquisition, J.C. All authors have read and agreed to the published version of the manuscript.

Funding: This work is supported by FCT, I.P./MCTES through national funds (PIDDAC): LA/P/0068/2020 (https://doi.org/10.54499/LA/P/0068/2020, accessed on 15 December 2025), UID/50019/2025-(https://doi.org/10.54499/UID/50019/2025, accessed on 15 December 2025), UID/PRR/50019/2025 (https://doi.org/10.54499/UID/PRR/50019/2025, accessed on 15 December 2025), UID/PRR2/50019/2025 (https://doi.org/10.54499/UID/PRR2/50019/2025, accessed on 15 December 2025).

Data Availability Statement: Data is contained within the article.

Acknowledgments: We are grateful to the European Centre for Medium-Range Weather Forecasts (ECMWF), which has made the ERA5 dataset freely available (https://doi.org/10.24381/cds.adbb2d47, accessed on 15 December 2025). Permanent GNSS RINEX files are available from https://servir.igeoe.pt/trimblepivotweb/ and ftp://ftp.dgterritorio.pt/ReNEP (both accessed on 15 December 2025). Low-cost GNSS RINEX files are available from the authors upon reasonable request. Radiosonde data is available at https://weather.uwyo.edu/upperair/sounding.shtml (accessed on 18 December 2025).

Conflicts of Interest: The authors declare no conflicts of interest.

References

1. Vaquero-Martínez, J.; Antón, M. Review on the Role of GNSS Meteorology in Monitoring Water Vapor for Atmospheric Physics. *Remote Sens.* **2021**, *13*, 2287. [CrossRef]
2. Mateus, P.; Catalão, J.; Fernandes, R.; Miranda, P.M.A. Atmospheric Water Vapor Variability over Houston: Continuous GNSS Tomography in the Year of Hurricane Harvey (2017). *Remote Sens.* **2024**, *16*, 3205. [CrossRef]
3. Flores, A.; Ruffini, G.; Rius, A. 4D Tropospheric Tomography Using GPS Slant Wet Delays. *Ann. Geophys.* **2000**, *18*, 223–234. [CrossRef]
4. Champollion, C.; Masson, F.; Bouin, M.N.; Walpersdorf, A.; Doerflinger, E.; Bock, O.; Van Baelen, J. GPS Water Vapour Tomography: Preliminary Results from the ESCOMPTE Field Experiment. *Atmos. Res.* **2005**, *74*, 253–274. [CrossRef]
5. Rohm, W.; Bosy, J. The Verification of GNSS Tropospheric Tomography Model in a Mountainous Area. *Adv. Space Res.* **2011**, *47*, 1721–1730. [CrossRef]
6. Benevides, P.; Nico, G.; Catalão, J.; Miranda, P.M.A. Bridging InSAR and GPS Tomography: A New Differential Geometrical Constraint. *IEEE Trans. Geosci. Remote Sens.* **2016**, *54*, 697–702. [CrossRef]
7. Gradinarsky, L.P. *Sensing Atmospheric Water Vapor Using Radio Waves*; Chalmers University of Technology: Göteborg, Sweden, 2002.
8. Chen, B.; Liu, Z. Voxel-Optimized Regional Water Vapor Tomography and Comparison with Radiosonde and Numerical Weather Model. *J. Geod.* **2014**, *88*, 691–703. [CrossRef]
9. Perler, D.; Geiger, A.; Hurter, F. 4D GPS Water Vapor Tomography: New Parameterized Approaches. *J. Geod.* **2011**, *85*, 539–550. [CrossRef]
10. Benevides, P.; Catalao, J.; Nico, G.; Miranda, P.M.A. 4D Wet Refractivity Estimation in the Atmosphere Using GNSS Tomography Initialized by Radiosonde and AIRS Measurements: Results from a 1-Week Intensive Campaign. *GPS Solut.* **2018**, *22*, 91. [CrossRef]
11. Miranda, P.M.A.; Mateus, P. A New Unconstrained Approach to GNSS Atmospheric Water Vapor Tomography. *Geophys. Res. Lett.* **2021**, *48*, e2021GL094852. [CrossRef]
12. Trzcina, E.; Rohm, W.; Smolak, K. Parameterisation of the GNSS Troposphere Tomography Domain with Optimisation of the Nodes' Distribution. *J. Geod.* **2022**, *97*, 2. [CrossRef]
13. Zhao, Q.; Zhang, K.; Yao, W. Influence of Station Density and Multi-Constellation GNSS Observations on Troposphere Tomography. *Ann. Geophys.* **2019**, *37*, 15–24. [CrossRef]
14. Mateus, P.; Zhang, M.; Catalão, J.; Miranda, P.M.A. Enhancing the Accuracy of GNSS Tomography with an Empirical Stochastic Model. *GPS Solut.* **2026**, *30*, 64. [CrossRef]
15. Marut, G.; Hadas, T.; Kaplon, J.; Trzcina, E.; Rohm, W. Monitoring the Water Vapor Content at High Spatio-Temporal Resolution Using a Network of Low-Cost Multi-GNSS Receivers. *IEEE Trans. Geosci. Remote Sens.* **2022**, *60*, 5804614. [CrossRef]
16. Xue, C.; Psimoulis, P.; Zhang, Q.; Meng, X. Analysis of the Performance of Closely Spaced Low-Cost Multi-GNSS Receivers. *Appl. Geomat.* **2021**, *13*, 415–435. [CrossRef]
17. Paziewski, J.; Hadas, T.; Rohm, W.; Wielgosz, P. Research on GNSS Positioning and Applications in Poland in 2019–2022. *Adv. Geod. Geoinf.* **2023**, *72*, 43. [CrossRef]
18. Aichinger-Rosenberger, M.; Wolf, A.; Senn, C.; Hohensinn, R.; Glaner, M.F.; Moeller, G.; Soja, B.; Rothacher, M. MPG-NET: A Low-Cost, Multi-Purpose GNSS Co-Location Station Network for Environmental Monitoring. *Measurement* **2023**, *216*, 112981. [CrossRef]
19. Wu, J.; Ma, H.; Wu, W.; Cheng, D. Monitoring Water Vapor Transport in near Real-Time with Low-Cost GNSS Receiver Network. *Sci. Rep.* **2025**, *15*, 24095. [CrossRef]
20. Bosser, P.; Ancelin, J.; Métois, M.; Rolland, L.; Vidal, M. Evaluation of Tropospheric Estimates from CentipedeRTK, a Collaborative Network of Low-Cost GNSS Stations. *GPS Solut.* **2024**, *28*, 158. [CrossRef]

21. Hamza, V.; Stopar, B.; Ambrožič, T.; Sterle, O. Performance Evaluation of Low-Cost Multi-Frequency GNSS Receivers and Antennas for Displacement Detection. *Appl. Sci.* **2023**, *11*, 6666. [CrossRef]
22. Hamza, V.; Stopar, B.; Ambrožič, T.; Turk, G.; Sterle, O. Testing Multi-Frequency Low-Cost GNSS Receivers for Geodetic Monitoring Purposes. *Sensors* **2020**, *20*, 4375. [CrossRef]
23. Hamza, V.; Stopar, B.; Sterle, O.; Pavlovčič-Prešeren, P. Low-Cost Dual-Frequency GNSS Receivers and Antennas for Surveying in Urban Areas. *Sensors* **2023**, *23*, 2861. [CrossRef] [PubMed]
24. Tunini, L.; Zuliani, D.; Magrin, A. Applicability of Cost-Effective GNSS Sensors for Crustal Deformation Studies. *Sensors* **2022**, *22*, 350. [CrossRef]
25. Romero-Andrade, R.; Trejo-Soto, M.E.; Vázquez-Ontiveros, J.R.; Hernández-Andrade, D.; Cabanillas-Zavala, J.L. Sampling Rate Impact on Precise Point Positioning with a Low-Cost GNSS Receiver. *Appl. Sci.* **2021**, *11*, 7669. [CrossRef]
26. Janos, D.; Kuras, P.; Chang, C.-M.; Chronopoulos, D. Evaluation of Low-Cost GNSS Receiver under Demanding Conditions in RTK Network Mode. *Sensors* **2021**, *21*, 5552. [CrossRef] [PubMed]
27. Krietemeyer, A.; van der Marel, H.; van de Giesen, N.; ten Veldhuis, M.-C. High Quality Zenith Tropospheric Delay Estimation Using a Low-Cost Dual-Frequency Receiver and Relative Antenna Calibration. *Remote Sens.* **2020**, *12*, 1393. [CrossRef]
28. Dabove, P.; Bagheri, M. Enhancing Atmospheric Monitoring Capabilities: A Comparison of Low- and High-Cost GNSS Networks for Tropospheric Estimations. *Remote Sens.* **2024**, *16*, 2223. [CrossRef]
29. Li, L.; Zhang, H.; Yuan, Y.; Aichinger-Rosenberger, M.; Soja, B. On the Real-Time Tropospheric Delay Estimates Using Low-Cost GNSS Receivers and Antennas. *GPS Solut.* **2024**, *28*, 119. [CrossRef]
30. Wu, J.; Chen, Y.; Bo, L.; Wu, W. Tropospheric Delay Retrieval Using Cost-Effective Single-Frequency GNSS Receivers with Established Reference Stations. *Measurement* **2025**, *241*, 115767. [CrossRef]
31. ReNEP | ReNEP. Available online: https://renep.dgterritorio.gov.pt/ (accessed on 17 February 2026).
32. Miranda, P.M.A.; Adams, D.K.; Tomé, R.; Fernandes, R.; Mateus, P. Optimizing Boundary Conditions in GNSS Tomography: A Continuous 7-Month Case Study in the Amazon. *Geophys. Res. Lett.* **2023**, *50*, e2023GL105030. [CrossRef]
33. Tomasi, C. Vertical Distribution Features of Atmospheric Water Vapor in the Mediterranean, Red Sea, and Indian Ocean. *J. Geophys. Res. Atmos.* **1984**, *89*, 2563–2566. [CrossRef]
34. Ding, N.; Zhang, S.; Wu, S.; Wang, X.; Kealy, A.; Zhang, K. A New Approach for GNSS Tomography from a Few GNSS Stations. *Atmos. Meas. Tech.* **2018**, *11*, 3511–3522. [CrossRef]
35. Hoffmann, L.; Günther, G.; Li, D.; Stein, O.; Wu, X.; Griessbach, S.; Heng, Y.; Konopka, P.; Müller, R.; Vogel, B.; et al. From ERA-Interim to ERA5: The Considerable Impact of ECMWF's next-Generation Reanalysis on Lagrangian Transport Simulations. *Atmos. Chem. Phys.* **2019**, *19*, 3097–3214. [CrossRef]
36. Stull, R. An Algebra-Based Survey of Atmospheric Science. In *Practical Meteorology: An Algebra-Based Survey of Atmospheric Science*; Sundog Publishing LLC: Madison, WI, USA, 2017; pp. 87–118.
37. GitHub—Wrf-Model/WRF: The Official Repository for the Weather Research and Forecasting (WRF) Model. Available online: https://github.com/wrf-model/WRF (accessed on 5 December 2025).
38. Hong, S.Y.; Lim, J.-O.J. The WRF Single-Moment 6-Class Microphysics Scheme (WSM6). *Asia. Pac. J. Atmos. Sci.* **2006**, *42*, 129–151.
39. Janjic, Z.I. The Step-Mountain Eta Coordinate Model: Further Developments of the Convection, Viscous Sublayer, and Turbulence Closure Schemes. *Mon. Weather Rev.* **1994**, *122*, 927–945. [CrossRef]
40. Iacono, M.J.; Delamere, J.S.; Mlawer, E.J.; Shephard, M.W.; Clough, S.A.; Collins, W.D. Radiative Forcing by Long-Lived Greenhouse Gases: Calculations with the AER Radiative Transfer Models. *J. Geophys. Res. Atmos.* **2008**, *113*, 13103. [CrossRef]
41. Tewari, M.; Chen, F.; Wang, W.; Dudhia, J.; Lemone, A.; Mitchell, E.; Ek, M.; Gayno, G.; Wegiel, W.; Cuenca, R. *Implementation and Verification of the Unified Noah Land-Surface Model in the WRF Model*; Oregon State University: Corvallis, OR, USA, 2004.
42. Mateus, P.; Nico, G.; Catalão, J. Uncertainty Assessment of the Estimated Atmospheric Delay Obtained by a Numerical Weather Model (NMW). *IEEE Trans. Geosci. Remote Sens.* **2015**, *53*, 6710–6717. [CrossRef]
43. Rohm, W. The Precision of Humidity in GNSS Tomography. *Atmos. Res.* **2012**, *107*, 69–75. [CrossRef]
44. Bender, M.; Dick, G.; Ge, M.; Deng, Z.; Wickert, J.; Kahle, H.G.; Raabe, A.; Tetzlaff, G. Development of a GNSS Water Vapour Tomography System Using Algebraic Reconstruction Techniques. *Adv. Space Res.* **2011**, *47*, 1704–1720. [CrossRef]
45. Wang, Y.; Ding, N.; Zhang, Y.; Li, L.; Yang, X.; Zhao, Q. A New Approach of the Global Navigation Satellite System Tomography for Any Size of GNSS Network. *Remote Sens.* **2020**, *12*, 617. [CrossRef]
46. Benevides, P.; Nico, G.; Catalao, J.; Miranda, P.M.A. Analysis of Galileo and GPS Integration for GNSS Tomography. *IEEE Trans. Geosci. Remote Sens.* **2017**, *55*, 1936–1943. [CrossRef]
47. Heublein, M.; Erik Bradley, P.; Hinz, S. Observing Geometry Effects on a Global Navigation Satellite System (GNSS)-Based Water Vapor Tomography Solved by Least Squares and by Compressive Sensing. *Ann. Geophys.* **2020**, *38*, 179–189. [CrossRef]
48. Shehaj, E.; Geiger, A.; Rothacher, M.; Moeller, G. Retrieval of Refractivity Fields from GNSS Tropospheric Delays: Theoretical and Data-Based Evaluation of Collocation Methods and Comparisons with GNSS Tomography. *J. Geod.* **2024**, *98*, 112. [CrossRef] [PubMed]

49. Haji-Aghajany, S.; Amerian, Y.; Verhagen, S.; Rohm, W.; Schuh, H. The Effect of Function-Based and Voxel-Based Tropospheric Tomography Techniques on the GNSS Positioning Accuracy. *J. Geod.* **2021**, *95*, 78. [CrossRef]
50. Izanlou, S.; Haji-Aghajany, S.; Amerian, Y. Enhanced Troposphere Tomography: Integration of GNSS and Remote Sensing Data with Optimal Vertical Constraints. *IEEE J. Sel. Top. Appl. Earth Obs. Remote Sens.* **2024**, *17*, 3701–3714. [CrossRef]
51. Zhang, B.; Fan, Q.; Yao, Y.; Xu, C.; Li, X. An Improved Tomography Approach Based on Adaptive Smoothing and Ground Meteorological Observations. *Remote Sens.* **2017**, *9*, 886. [CrossRef]
52. Saxena, S.; Dwivedi, R. GNSS Ground-Based Tomography: State-of-the-Art and Technological Challenges. *Int. J. Remote Sens.* **2023**, *44*, 5313–5343. [CrossRef]
53. Zhao, Q.; Ma, X.; Yao, Y. Preliminary Result of Capturing the Signature of Heavy Rainfall Events Using the 2-d-/4-d Water Vapour Information Derived from GNSS Measurement in Hong Kong. *Adv. Space Res.* **2020**, *66*, 1537–1550. [CrossRef]
54. Mateus, P.; Miranda, P.M.A. Using InSAR Data to Improve the Water Vapor Distribution Downstream of the Core of the South American Low-Level Jet. *J. Geophys. Res. Atmos.* **2022**, *127*, e2021JD036111. [CrossRef]

Disclaimer/Publisher's Note: The statements, opinions and data contained in all publications are solely those of the individual author(s) and contributor(s) and not of MDPI and/or the editor(s). MDPI and/or the editor(s) disclaim responsibility for any injury to people or property resulting from any ideas, methods, instructions or products referred to in the content.